PERGAMON

Journal of Quantitative Spectroscopy & Radiative Transfer 65 (2000) 367–385

Journal of Quantitative Spectroscopy & Radiative Transfer

www.elsevier.com/locate/jqsrt

# X-ray radiation from matter in extreme conditions

A. Maksimchuk[a,*], M. Nantel[a], G. Ma[a], S. Gu[a], C.Y. Côté[a], D. Umstadter[a], S.A. Pikuz[b], I.Yu. Skobelev[c], A.Ya. Faenov[c]

[a]*Center for Ultrafast Optical Science, University of Michigan, 1006 IST Building, 2200 Bonisteel, Ann Arbor, MI 48109-2099, USA*

[b]*P.N. Lebedev Physics Institute, Russian Academy of Science, Moscow, 11792, Russia*

[c]*Multi-Charged Ion Spectral Data Center, VNIIFTRI, Moscow Region, 141570, Russia*

**Abstract**

We study transient atomic and plasma processes in the new parameter regime of hot dense matter, produced by an intense ultrashort laser pulse. Specifically, we study the effects of extremely high fields on ion electronic structure. These high fields are achieved in either of two ways: (1) by the field of unscreened ion charges in a plasma ($\sim 10^9$ V/cm), which result in strongly coupled effects such as continuum lowering, line broadening and line-merging, or (2) by the high electromagnetic field of an intense laser ($\sim 10^{11}$ V/cm), which results in the formation of laser satellites around forbidden X-ray lines. 

## 1. Introduction

The advent of compact high-intensity subpicosecond lasers, based on chirped-pulse-amplification (CPA) technique [1,2] gives access to a new regime of laser–matter interaction. First of the most important features of this interaction is a short laser pulse duration — shorter than the typical hydrodynamic plasma expansion time — that allows for the clean subpicosecond laser pulses to deposit their energy at a solid density. Much of the attention has been focused on attaining high-density/high-temperature plasmas with CPA laser to generate short pulses of X-ray [3–6]. The ultrashort-laser pulses can also create very dense but colder strongly coupled plasmas (SCPs),

* Corresponding author. Tel.: + 001-734-763-6007; fax: 001-734-763-4876.
*E-mail address:* tolya@umich.edu (A. Maksimchuk)

0022-4073/00/$ - see front matter 
PII: S0022-4073(99)00081-3

whose properties challenge the very definition of plasmas [7]. The second feature of this interaction is the extremely high radiation pressure on the surface of the solid target which can reach for the laser intensity of $10^{18}$ W/cm$^2$ a few hundred megabars. When interacting with the underdense plasma ($n_e \lesssim n_c$, where $n_c$ is a critical plasma density for the laser wavelength $\lambda_0$) the radiation pressure can push the plasma into the target [8], producing a crater and leading to hole boring [9]. In the case when the plasma gradient is significantly less than the laser wavelength, the radiation pressure acts like a piston on a solid target producing a strong shock wave, which can compress the material to several times the initial density.

The experiments presented in this paper have been done with high-intensity ultrashort laser pulses. Here we demonstrate the effect of near solid density plasma on the emission spectra of multicharged ions in keV spectral region that results in continuum lowering, significant line broadening and line merging. Using time-resolved spectroscopy in XUV spectral region we study also the dynamic of continuum lowering and line merging of SCPs over wide range of densities and temperatures which provides a testbed for atomic physics models of such plasmas. We illustrate also the influence of strong oscillating electrical fields produced by a high-intensity laser on the emission characteristics of the He-like ions that results in appearance of laser-induced satellites of the forbidden transitions in keV spectral region.

## 2. Effects of high-fields from plasma charges

### 2.1. Continuum lowering, line broadening and line merging in solid density plasmas

Progress in high-intensity short pulse lasers now allows routinely to generate pulses with a peak power in excess of a terawatt level and a petawatt peak power threshold has been achieved [10,11]. Such laser systems open the possibility to study phenomena produced by high-intensity radiation in plasmas whose density is orders of magnitude higher than the plasma critical density $n_c = 1.1 \times 10^{21}/\lambda_0^2$ cm$^{-3}$, where $\lambda_0$ is the wavelength in micron. When the focused intensity exceeds $10^{18}$ W/cm$^2$, the laser–matter interaction becomes strongly nonlinear due to the influence of strong radiation pressure:

$$P_{rad} = (1 + R)E_0^2/8\pi = (1 + R)3.3 \times 10^2 I_{18} \text{ (Mbar)}, \tag{2.1}$$

where $R$ is the reflection coefficient and $I_{18}$ is the laser intensity in units of $10^{18}$ W/cm$^2$. It follows from this equation that the light pressure at the intensities $I_r = 10^{18}$ W/cm$^2$ reaches $3.3 \times 10^2$ Mbar. This pressure is comparable to the thermal pressure $P = n_e k T_e$ (where $n_e$ and $T_e$ are electron density and temperature) of the solid density plasma with the temperature of a few hundred electron volts. So, the radiation pressure of ultra-high-intensity laser pulses with negligible prepulse can maintain the initial steep gradient scale length ($L \ll \lambda$) and confine or even compress the plasma. This near solid density plasma [5,12–15], confined by the radiation pressure [16] can serve as a source of the ultrafast X-ray pulses or fast particles. Production of matter with such parameters in a laboratory is of great interest for astrophysics [17–19], conventional [20] and advanced ICF studies [21] and for the physics of strongly coupled plasmas [22].

In the present experiments we combine very high laser intensities with ultrashort gradient-scale length plasmas. To avoid plasma expansion before main pulse arrival and to produce a solid density plasma, a high contrast ultrashort laser pulse has to be used. The experiments were carried out with the hybrid Ti : sapphire/Nd : phosphate glass CPA laser at the University of Michigan. The laser is able to deliver up to 4 J in 400 fs pulse at the wavelength of 1.053 μm with the intensity contrast ratio of $5 \times 10^5$ to 1, as measured with a 3rd order autocorrelation technique. The contrast has been improved to an estimated $10^{10}$ to 1 by the frequency doubling of laser light in 4 mm KDP crystal. The maximum conversion efficiency to a 0.53 μm light was about 80%. Because of the nonlinear distortion of the laser wavefront in a doubling crystal, in these experiments we were limited to the energy of $\sim 1$ J in a second harmonic. The laser beam was focused on a surface of solid magnesium target at 45° incidence angle with $f/3$ off-axis parabolic mirror. The maximum focused intensity was $2 \times 10^{18}$ W/cm$^2$. To produce a long gradient scale plasma we used Michelson interferometer to create two identical collinear 0.53 μm laser beams with the relative time delay of 100 ps and a focused intensity of $10^{18}$ W/cm$^2$ in each pulse. We used X-ray spectroscopy to study the high-density effects on the emission of the multiply charged ions. For the described experiment we coupled a spherically bent (the radius of curvature $R = 186$ mm) mica crystal spectrometer ($2d = 19.84$ Å) with a X-ray CCD camera. This spectrometer has a spectral resolution of $\lambda/\Delta\lambda \geq 5000$, a luminosity $\sim 100$ times higher than the flat crystal spectrometer, and a spatial resolution of order a ten microns. It should be noted that the use of the X-ray CCD and illumination of the target with a prepulse provided a very convenient and precise way for the wavelength referencing.

We recorded time integrated spectra from magnesium plasma in the vicinity of the resonance $He_\alpha$ line and Li-like satellites, as well as He-like $1s^2$–$1snp$ ($n \geq 3$) series for illumination of the target with the prepulse and for the high contrast illumination (Fig. 1). In the first case the identified lines are the $He_\alpha$ resonance transition ($1s^2\ ^1S_0$–$1s2p^1P_1$), intercombination transition ($1s^2\ ^1S_0$–$1s2p^3P_1$) and Li-like satellites ($1s^22l$–$1s2l2l'$) (Fig. 1a). This spectrum looks similar to the spectra obtained for the plasma interacting with long (0.1–1 ns) laser pulses, while the spectrum at high contrast illumination is very different. In the latter case we observed significant broadening of $He_\alpha$ line, disappearance of intercombination line (that can serve as evidence for the high density of the plasma) and merging of Li-like satellites lines. We found also that the intensity of $He_\alpha$ line was reduced by factor of five. Even more drastic changes are observed when comparing emission of He-like $1s^2$–$1snp$ ($n \geq 3$) series for these two cases (Fig. 1b). For the illumination with the prepulse the identified lines are $He_\beta$ ($1s^2\ ^1S_0$–$1s3p^1P_1$) line, $He_\gamma$ ($1s^2\ ^1S_0$–$1s4p^1P_1$) line, $He_\delta$ ($1s^2\ ^1S_0$–$1s5p^1P_1$) line, H-like $Ly_\beta$ ($1s^2S_{1/2}$–$3p^2P_{1/2,3/2}$) lines and Li-like dielectronic satellites ($1s^23l$–$1s3l3l'$). All the lines are very distinct and narrow. With a high contrast illumination we found significant broadening of $He_\beta$ line to FWHM of 100 mÅ (it was possible that this line was merged with dielectronic satellites on the red side) and found that $He_\gamma$ and $He_\delta$ lines have disappeared. The spectra also shows strong bound-free continuum radiation. All these feature can be attributed to the effects of high density in a subpicosecond laser produced plasma.

Using an ion-cell continuum lowering model [23] we estimated the electron density from the ionization potential depression $\Delta E$:

$$\Delta E_{\mathrm{IC}} = Ze^2/r_{\mathrm{i}}, \quad r_{\mathrm{i}} = (3/4\pi N_i)^{1/3} \tag{2.2}$$

where $Z$ is the charge of the emitting ion, $r_{\mathrm{i}}$ is the ion sphere radius, and $N_i$ is the ion density. In Fig. 2 the dependence of the ionization potential depression for MgXI ion is plotted as a function of

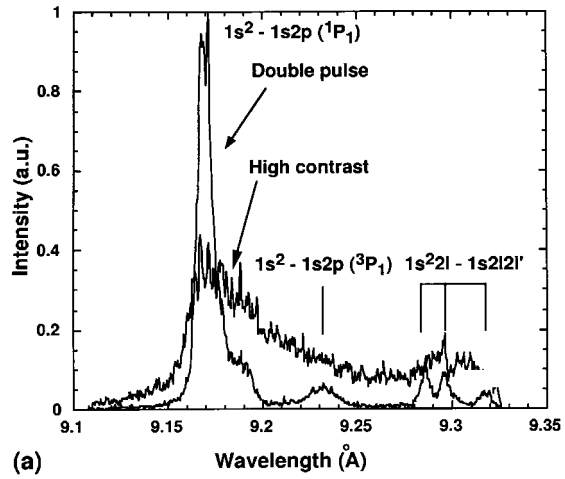


Fig. 1. Time integrated emission spectra of a magnesium plasma produced by high-intensity laser pulse with a prepulse and for high contrast laser illumination of the target: (a) in the vicinity of He-like resonance, intercombination and Li-like satellite lines (the intensity of the spectrum for high contrast illumination is multiplied by 2 for better viewing) and (b) in the vicinity of He-like $1s^2$–$1snp$ lines. Spectrum for the high contrast illumination is shifted vertically for better viewing.

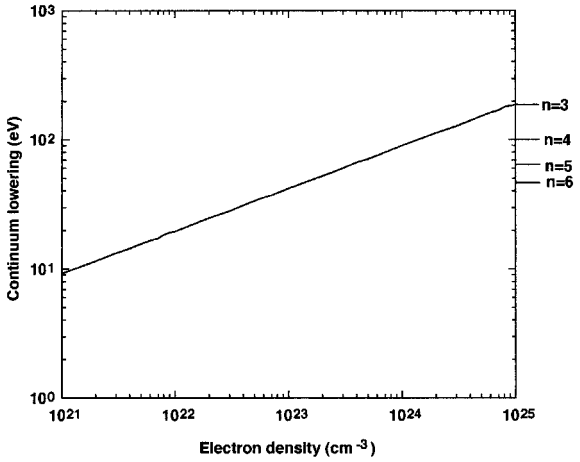


Fig. 2. Ionization potential depression for He-like Mg ion as a function of electron density using ion-cell model. On the right vertical axis are the positions of the principal quantum numbers $n$ ($3 \leq n \leq 6$) in He-like magnesium.

the electron density. To merge the $He_\delta$ line into continuum the ionization potential should be depressed by $\Delta E \simeq 66$ eV, that corresponds to the electron density of $\sim 3\times10^{23}$ cm$^{-3}$, while merging of the $He_\gamma$ line ($\Delta E \simeq 102$ eV) occurs at an electron density of $\sim 1.5\times10^{24}$ cm$^{-3}$.

To account for plasma microfield fluctuation effects in a simple manner, the Inglis–Teller limit [24] in the formulation of More [25] can be used:

$$I_p - E_n \leq \Delta E_{IT} < I_p - E_{n-1},$$
$$E_{n+1} - E_n \simeq r_n(Ze^2/r_i^2), \quad r_n = a_0 n^2/Z, \tag{2.3}$$

where $n$ is the principal quantum number, $E_n$ is the energy of the $n$th level, $a_0$ is the Bohr radius and $I_p$ is the ionization potential. The Inglis–Teller limit predicts the density at which the Stark broadening of two adjacent levels $n$ and $n+1$ is more than the energy separating them, effectively when they merge. The last identifiable level is then the one with quantum number $n-1$, and the amount of lowering $\Delta E_{IT}$ is given by the first line in Eq. (2.3). An estimate of the electron density from Inglis–Teller line merging model gives the values of the electron density close to that given by the ion-cell model. If $He_\varepsilon$ ($1s^2S_0$–$1s6p^1P_1$) and $He_\delta$ lines are merge than $n_e \simeq 2\times10^{23}$ cm$^{-3}$. In the case of $He_\delta$ and $He_\gamma$ line merging the corresponding density will be above the solid density $n_e \simeq 10^{24}$ cm$^{-3}$. Of course, such simple models, can give only rough estimate of the electron density, nevertheless they show that the near solid density plasma can be formed with the ultrashort laser pulses.

A more detailed theoretical analysis that includes the dielectronic satellites emission and Stark broadening [26] showed that both spectra (Fig. 1a and b) at high contrast illumination can be fitted with the electron density $n_e = 3-4\times10^{23}$ cm$^{-3}$ and electron temperature $T_e = 200$–$300$ eV. This value of electron density is $\sim 70$–$95\%$ of the solid density magnesium plasma with the average charge $\bar{Z}=10$, which is $4.3\times10^{23}$ cm$^{-3}$. To the our knowledge this is the highest inferred electron density of the hot plasma, produced by high-intensity ultrashort laser pulse. It should be pointed out that such high plasma density was determined from the time integrated spectra, so the peak of the electron density may be even higher.

These results suggest that the radiative pressure plays an important role in interaction of relativistic-intensity, high-contrast laser pulses with plasma, altering the plasma expansion and even compressing a solid density plasmas.

### 2.2. Continuum lowering and line merging in strongly coupled plasmas

Strongly-coupled plasmas (SCPs) are found in stellar and jovian planet interiors [27], inertial confinement fusion (ICF) pellets [28,29] and are essential for a thorough understanding of compressed material equations-of-state [30,31]. These plasmas are characterized by high densities and/or relatively low temperatures, such that the Coulomb potential energy between the particles exceeds their kinetic energy, and thus the coupling parameter $\Gamma = (Z^2e^2)/(r_i kT)$ (where $r_i$ is the ion-sphere radius) is larger than one.

Experimental studies of strongly coupled plasmas are difficult due to the need to simultaneously obtain and diagnose high-density/low-temperature conditions. Consequently, very little quantitative experimental work on the subject [32,33] has been done up to now. The strong Coulomb fields can dramatically perturb the atomic structure of the ions — and in turn their ionization, emissivity and opacity — through various process. In laser–matter interactions, pressure ionization has been observed in shocked solids through shifts in photo-absorption edges [30,32,34], and in ablation plasmas through the disappearance of emission lines [12,28,33,35], where it has been used as a density diagnostic. However, these data are usually time-integrated or space-integrated, or both, which prohibits controlled studies of dynamics under the rapidly varying conditions of laser-produced plasmas and limits the accuracy of the density diagnostic. Finally, experiments providing precise data for model validation are rare, and the few that have been reported involved plasmas that, in addition to their limited density and temperature ranges, were restricted to the

intermediately coupled regime ($\Gamma \leq 0.2$) [33]. Here we present XUV spectra emitted from strongly coupled laser-produced carbon plasmas, making use of several essential innovations: (1) recent advances in short-pulse lasers [36] to couple the laser energy at nearly solid density, (2) imaging spectroscopy to achieve $\mu$m-scale spatial resolution, and (3) a jitter-free X-ray streak camera [37,38] to ensure both a high-signal-to-noise ratio and high ($\sim$ps) temporal resolution.

The experiments were conducted with a 10 Hz, 100 fs Ti : sapphire laser. Pulses of 50 mJ in energy at 780 nm were focused with a $MgF_2$ lens to an intensity of $10^{17}$ W/cm$^2$ on rotating solid carbon disk targets. The experimental setup is shown in Fig. 3. As pointed out in a previous section the use of subpicosecond pulses has the advantage of depositing the energy impulsively, in a thin target layer. Thus, the measurements are conducted after the laser pulse, in a freely decompressing ionized material. The emission spectra from the target were recorded with a grazing-incidence flat-field imaging XUV spectrometer coupled to an X-ray streak camera with a CCD readout, with a spatial resolution of 80 μm in the direction normal to the target plane and a spectral resolution of 0.15 Å. The subpicosecond X-ray streak camera [38] was coupled to a jitter-free averaging sweep system [37], consisting of two photoconductive switches triggered by part of the laser beam to sweep the plates of the camera at 10 Hz, in synchronization with the target emission. This novel technique — used for the first time here for spectroscopy — significantly extends the dynamic range of the streak camera and increases the signal-to-noise ratio. We were able to average the XUV spectrum over 600 shots with a temporal resolution of 4 ps, limited by a residual jitter of $\pm$ 2 ps. The laser contrast was improved by a factor of more than 100 over the

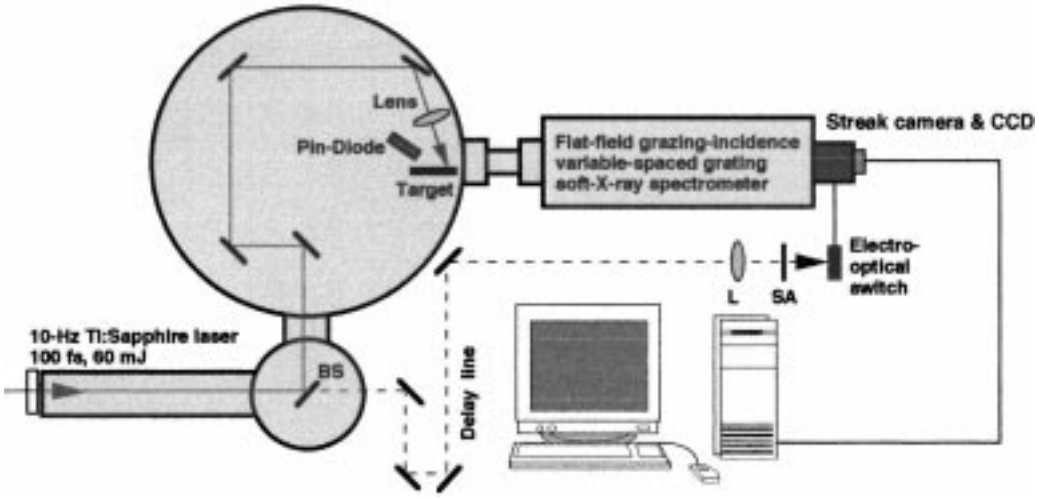


Fig. 3. Experimental setup. Most of the laser energy is sent to the target (T) on which it is focused by a lens (L). The emission from the expanding plasma plume is spatially resolved in the direction normal to the target and spectrally dispersed by the flat-field grazing incidence XUV spectrometer onto the slit of the streak camera. The data acquisition is done with a CCD camera. For the carbon experiment, the streak camera was operated in "jitter-free" mode: a small part of the laser energy was separated by a beam-splitter (BS), and sent through a variable delay line (DL) to a photoconductive switch (PS) to trigger the sweep of the camera. A lens (L) was used to focus the trigger beam through a saturable absorber (SA) to an optical fiber relay system (OF) for the photoconductive switch. PD stands for P-I-N diode.

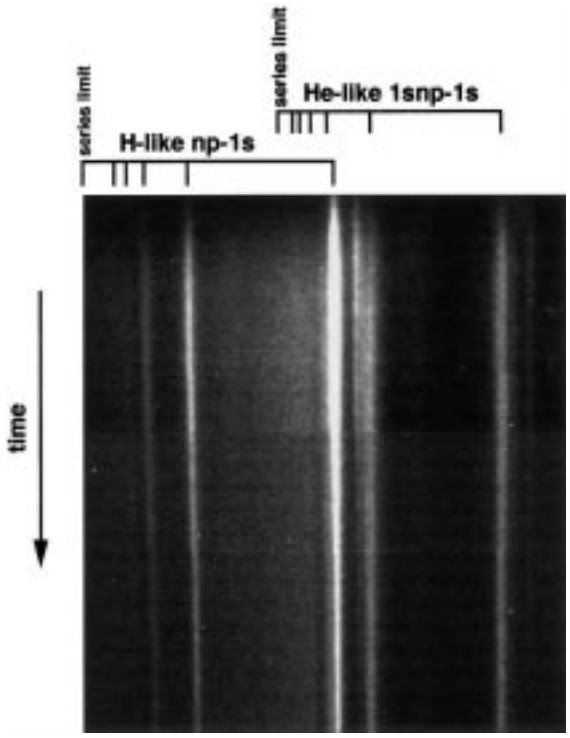


Fig. 4. Time-resolved XUV spectrum of a carbon plasma. This image is a composite of three experiments, each of which is the accumulations of 600 laser shots on the jitter-free X-ray streak camera.

typical figure of $10^5$ for Ti:sapphire lasers through high-energy seeding of clean pulses in the regenerative amplifier [36].

We present data from the 80 μm region closest to the target plane. Fig. 4 shows a composite time-resolved spectrum made from three different 600-shot exposures, showing the first 150 ps of emission. Because the streak camera was operated with a sweep speed of 7 ps/mm, a given exposure had a temporal window of only 90 ps. We scanned this time window from 0 to 225 ps by varying the optical delay of the laser beam triggering the streak camera. The jitter-free set-up hence gives us an absolute temporal calibration between each time window. The spectral resolution is 0.15 Å and the spectrum features the full $np$–1$s$ series from He-like and H-like ions, from 25 to 45 Å, as well as some Li-like and He-like satellites. There is considerable free-bound continuum radiation ending at the He-like edge near the H-like $2p$–1$s$ line. It is the position of this feature, along with the appearance of emission from the higher-$n$ levels of the H-like and He-like series, that are used for the continuum lowering analysis and plasma diagnostics.

Fig. 5 shows three line-outs between 25 and 37 Å taken at 0, 50 and 225 ps. These line-outs are integrated over 4 ps. The vacuum ionization potential (IP) of the He-like ion is marked at 31.62 Å (392.09 eV), and the He-like radiative recombination continuum and edges are sketched in bold lines. The position of the continuum edge (marked by vertical dashed lines for each spectrum) is determined to $\simeq$ 0.4–0.7 Å, limited by the presence of the bound–bound emission lines masking the

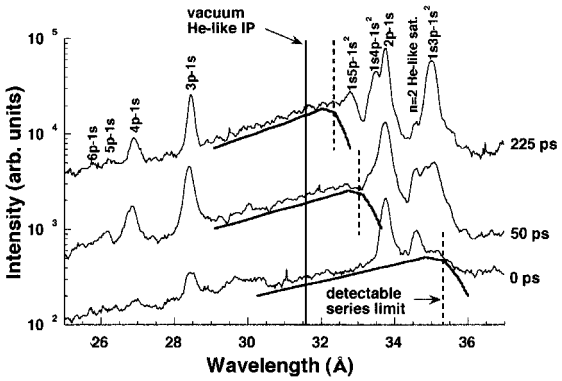


Fig. 5. Line-outs from the time-resolved spectra taken at $t = 0$,50 and 225 ps. The wavelength range is reduced to $25 < \lambda < 37$ Å for better emphasis on the spectral region involving the continuum lowering. The free-bound continuum and its edge are drawn on each line-out and the He-like ionization potential for vacuum and plasma conditions are marked by the vertical line. The three line-outs are offset vertically for better viewing.

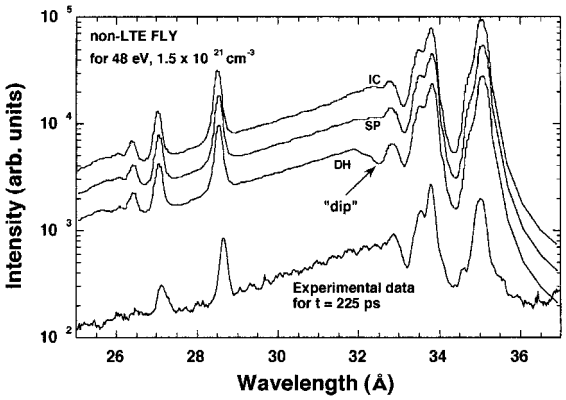


Fig. 6. Comparison of a line-out at $t = 225$ ps and non-LTE FLY simulations at 48 eV (determined from the slope of the continuum) and $1.5 \times 10^{21}$ cm$^{-3}$. Three different artificial spectra are shown, corresponding to the cases where the continuum lowering is calculated with the ion-cell (IC, long dashes), Stewart–Pyatt (SP, solid) and Debye–Huckel (DH, short dashes) models. Note the conspicuous "dip" in the DH spectra near the He-like series limit. The line-outs are offset vertically for better viewing.

exact position of the edge. The position of the continuum edge is measured to move from 35.3 Å (351.3 eV) at 0 ps, to 33.0 Å (375.2 eV) at 50 ps, and to 32.3 Å (383.6 eV) at 225 ps. The separation between the vacuum IP and the continuum edge for each spectrum indicates the amount of continuum lowering, which can be as high as 40.8 eV, or more than 10% of the IP for the spectrum at 0 ps. To the best of our knowledge, this is the highest percentage of continuum lowering recorded to date in a laboratory plasma, indicating the existence of a strongly-coupled system. This observation is supported by the absence of the He-like $1s3p$–$1s^2$ line at 0 ps, suggesting that the continuum extends below the $n = 3$ levels, leaving only $n = 2$ states available for the bound excited electrons. The strong dielectric satellites to the H-like $2p$–$1s$ line indicate that the plasma is recombining, which should favor the population of the higher-$n$ states of the He-like ions. Nevertheless, no resonance lines from the He-like series are detected at 0 ps save the strong $2p$–$1s$ transitions, and all the readily identifiable satellites to the H-like $2p$–$1s$ line originate from $n = 2$ doubly excited states. Qualitatively, from a continuum lowering standpoint, as the plasma evolves with time, the density — and hence the pressure — gradually decreases and the ionic potential is less and less perturbed: emission from higher-$n$ states reappear gradually, as is observed at 50 ps (He-like $1s3p$–$1s^2$ clearly present and $1s4p$–$1s^2$ visible in the H-like $2p$–$1s$ low-wavelength shoulder) and at 225 ps (He-like $1s4p$–$1s^2$ and $1s5p$–$1s^2$ are clearly identifiable). Effectively, the atomic structure changes gradually from mostly conduction-band-like, with few core levels available to the bound electrons, to mostly valence-band-like as it is for ions in dilute plasmas. A similar trend is observed in the higher-$n$ H-like emission lines, with the strengthening of the $3p$–$1s$ and $4p$–$1s$ lines, and the appearance of the $5p$–$1s$ and $6p$–$1s$ at later times, despite the falling temperature evident from the steepening of the continuum slope.

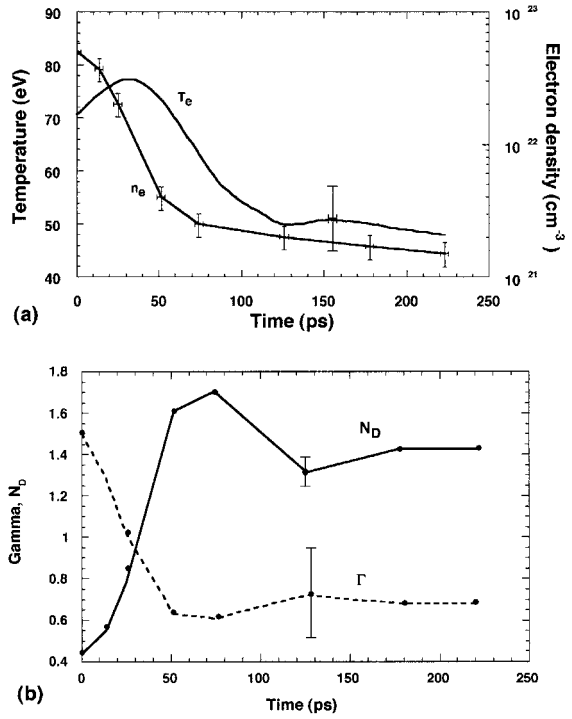


Fig. 7. Conditions as a function of time: (a) electron density and temperature; (b) coupling parameter $\Gamma$ and number of particles in the Debye sphere $N_D$.

For a more quantitative analysis of the plasma conditions, we extracted the electron temperature and density from the experimental spectra. This allows us to characterize the Coulomb coupling and compare the experimental continuum lowering to that calculated using the ion-cell [23], Debye-Huckel [19], and Stewart–Pyatt [39] with the line merging of the Inglis–Teller [24] models. We first established the electron temperature by the slope of the He-like continuum. We then generated artificial spectra using steady-state non-LTE FLY simulations [40]. The artificial spectra include instrumental broadening, average-field continuum lowering, Stark broadening and opacity. After that we found matches for the experimental spectra by varying the density in the simulation. This was done for eight line-outs at times 0, 14, 25, 50, 75, 125, 175 and 225 ps after the start of the emission. Fig. 6 gives examples of such matches for experimental line-outs at $t = 225$ ps, and a comparison of artificial spectra obtained with the different pressure ionization models. While the ion-cell (long-dashes) and Stewart–Pyatt (solid) models give almost indistinguishable fits for similar densities, we found it impossible to properly match artificial spectra generated with Debye–Huckel pressure ionization (short dashes), regardless of the choice of density. The "dip" in the spectrum near the series limit for the Debye–Huckel case is caused by an overestimation of the continuum lowering, leaving no merged bound-bound transitions to contribute to the spectrum in that region. This disagreement — the first time one can spectroscopically differentiate between continuum lowering models — is due to the strongly-coupled nature of the plasma which, as will come clear in the next figure, precludes the use of models based on the Debye–Huckel formalism.

The dynamics of the electron temperature and density is plotted in Fig. 7a for the first 225 ps of the emission. A peak density of $5 \times 10^{22}$ cm$^{-3}$ is inferred, which corresponds to one-tenth of the solid density for carbon with an average ionization $Z = 4.5$. It is not surprising that the electron density is less than that of a solid, as a $10^{17}$ W/cm$^2$ intensity on target with a $10^7$ contrast ratio will produce some preplasma from the $10^{10}$ W/cm$^2$ irradiation in the ns-scale pedestal. The temperature ranges from 50 to 80 eV, and this relatively low temperature with the high-densities combine to produce the strong Coulomb coupling, as is evident from Fig. 7b, which plots the coupling parameter, $\Gamma$, and the number of particles in the Debye sphere, $N_D$. Up to $t \simeq 30$ ps, the Debye sphere contains less than one particle on average, and this number stays below two in the first 225 ps. Similarly, the ratio of potential-to-kinetic energies hovers around one for the duration of the observation. Under these conditions, the concept of a Debye sphere has little statistical significance: the positive charges are not adequately shielded by electrons and Coulomb collisions dominate the ionized gas, which then cannot be correctly referred to as a plasma. This should be reflected in the continuum lowering, which should be better described by the models including the effect of the fluctuating microfields.

Fig. 8 shows the dynamics of the experimental continuum lowering. This is compared to the lowering calculated with the ion-cell (IC), Stewart–Pyatt (SP) models and the line merging model of Inglis–Teller (IT) models using the diagnostics from Fig. 7a. The uncertainty in the IT values corresponds to the energy difference between the last unmerged and the first merged levels. The areas shown for the IC and SP include the uncertainty in the density, the temperature and an ionization state between 4 and 5. The error bars on the measured continuum lowering includes the uncertainty in the position of the edge. The lowering predicted by the IC and SP models is

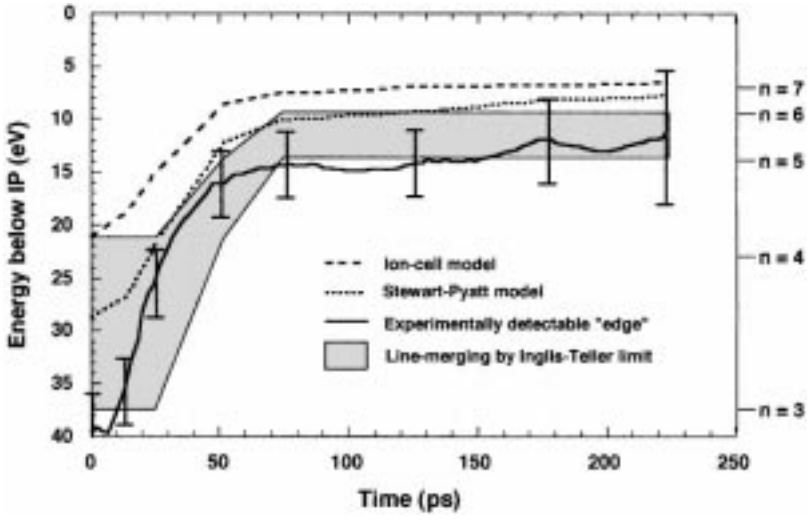


Fig. 8. Continuum lowering dynamics. The experimental continuum lowering is plotted (solid line) with a 4 ps resolution and error bars at eight times (0, 14, 25, 50, 75, 125, 175 and 225 ps after the start of the emission). The experimental lowering is compared to that calculated with the ion-cell, Stewart–Pyatt and Inglis–Teller models using the densities and temperatures from Fig. 7a. On the right vertical axis we give the position of the principal quantum number $n$ in He-like carbon.

consistently smaller than the experimental measurements. We attribute this discrepancy to the fact that in the experiment one cannot distinguish between the lowering of the ionization potential or the merging of the still bound–bound transitions. Therefore, the more realistic model for the spectra of strongly coupled systems is the Inglis–Teller line merging model, which includes the contributions from the fluctuating fields, as we can see from its good agreement with the experimental results.

In summary, using time resolved XUV spectroscopy we followed the transition of ultrashort laser produced carbon plasma from being a strongly coupled Coulomb system, with less than one particle in the Debye sphere for the first 30 ps ($\Gamma = 1.5$), to being a intermediately coupled plasma ($\Gamma = 0.5$). The atomic structure is seen to go from mostly conduction-band-like at early times when it was nearly solid density (maximum continuum lowering of more than 40 eV in He-like carbon, corresponding to more than 10 % of the ionization potential), to mostly valence-band-like when it was nearly gaseous density (continuum lowering of just $\simeq 3\%$ of the IP). Comparisons of the experimental spectra with numerical simulations validate the use of the Inglis–Teller limit for line-merging.

## 3. Effects of high-fields from intense laser pulses in plasmas

Strong harmonically oscillating electrical fields applied to the plasma can greatly influence the emission characteristics of the ions, producing satellite of the spectral lines. The source of these fields can be the plasma waves [41,42] or a strong radiation field, produced by high-intensity laser [43–46]. In the latter case, the nature of the satellites is a nonlinear interaction of the high power radiation with the excited states of the ions and is similar to anti-Stokes Raman scattering and stimulated two-photon emission [43]. These processes result in the conversion of the laser photons $\hbar\omega_L$ into photons $\hbar\omega'$ with the frequencies $\omega' = \omega_{fg} \pm \omega_L$, where $\omega_{fg}$ is the difference of the energies of the ion in the states $f$ and $g$ (Fig. 9). Such nonlinear processes are possible if the states $f$ and $g$ of the ion possess the same parity. This means that the transition $f \to g$ itself is optically forbidden.

Thus a laser field with frequency $\omega_L$ should produce two new spectral lines (so called laser satellites) around each parity-forbidden transition $f \to g$ of the ion. It should be noted that if the ion is multiply charged, then, (i) the wavelength of the emitted laser satellites can lie in the X-ray region of the spectrum, (ii) laser satellites have virtually the same intensities and (iii) the probabilities of the nonlinear processes become quite high only in ultra-high laser fields. The spectroscopy of laser satellites is important for ultra-high intensity lasers–matter interaction because it can provide information on the electric field strength in a plasma.

In the experiment described below, the X-ray spectra were excited by irradiation of solid targets of magnesium and aluminum with a 400 fs laser pulse with energy up to 1 J at the fundamental frequency ($\lambda_0 = 1.053$ μm) and intensity on a target up to $\sim 10^{18}$ W/cm$^2$ with the contrast ratio of $5 \times 10^5$ to 1. A spherically curved mica crystal (with the radius of curvature $R = 186$ mm) focused the spectrally dispersed plasma radiation onto the photocathode of an X-ray streak camera in a slitless arrangement (Fig. 10). The spectral resolution of the system in the dynamic regime was $\lambda/\Delta\lambda \geq 5000$. The time resolution at the maximum sweep speed was equal to 5 ps. The image from the X-ray streak camera screen was intensified with a microchannel plate and read out with 12 bit

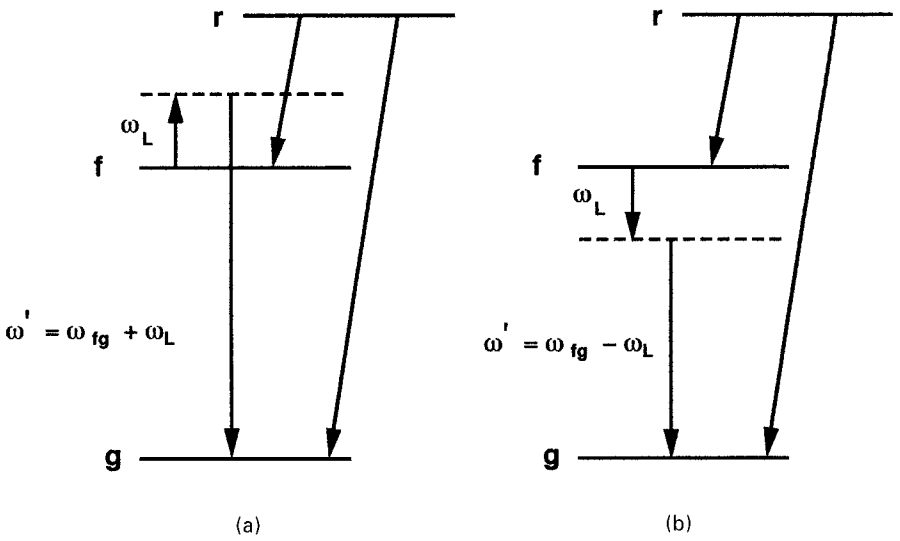


Fig. 9. Scheme of the laser induced two-photon processes (a) anti-Stokes Raman scattering and (b) stimulated two-photon emission.

visible CCD camera, which made possible wavelength referencing of the spectrograms obtained in different shots. In the present experiment the relative arrangement of the plasma, the spherical crystal and the detection system was chosen to record the emission spectrum in the ranges 9.15–9.35 Å (in the second order of reflection from the mica crystal) and 6.1–6.23 Å (in the third order of reflection). In the case of the magnesium plasma this made it possible to observe the resonance and intercombination lines of the He-like Mg XI and their dielectronic satellites and, in the case of aluminum plasma, the $1s5p\,^1P_1$–$1s^2\ ^1S_0$ line of the He-like ion Al XII. The interaction of laser photons $\hbar\omega_L = 9524\ \mathrm{cm}^{-1}$ with $1s2s\,^1S_0$ state of MgXI ion should produce two satellite lines with wavelength $\lambda_{s1} \approx 9.2178$ Å and $\lambda_{s2} \approx 9.2341$ Å, since according to calculation performed in Ref. [39], the energy of $1s2s\,^1S_0$ level equals $1.0839 \times 10^7\ \mathrm{cm}^{-1}$. The laser satellites formed from $1s5s\,^1S_0$, and $1s5d\,^1D_2$ states of the Al XII ion should also fall in the indicated detection range. The intensity of laser satellites can be estimated following the approach of Ref. [43]:

$$P_{s1,s2} = \omega'/\omega_L N_f I_L \sigma, \tag{3.1}$$

where $N_f$ is the population density in the upper level of a forbidden transition, $I_L$ is the laser intensity and $\sigma$ is the Raman scattering cross section. In the approximation of one virtual level $\sigma$ can be estimated according to formula:

$$\sigma = \frac{\omega_L \omega'^3 (\omega_{rf} + \omega_{rg})^2 f_{gr} f_{fr}}{4(\omega_{rf} - \omega_L)^2 (\omega_{rg} + \omega_L)^2 \omega_{rg} \omega_{rf}} \sigma_T \tag{3.2}$$

where $\sigma_T = 8\pi/3/(e^2/mc^2)$ is the Thomson scattering cross section, and $f_{gr}$, $f_{fr}$ are the absorption oscillator strengths from ground state $g$ and the metastable level $f$ to the resonance level $r$, respectively.

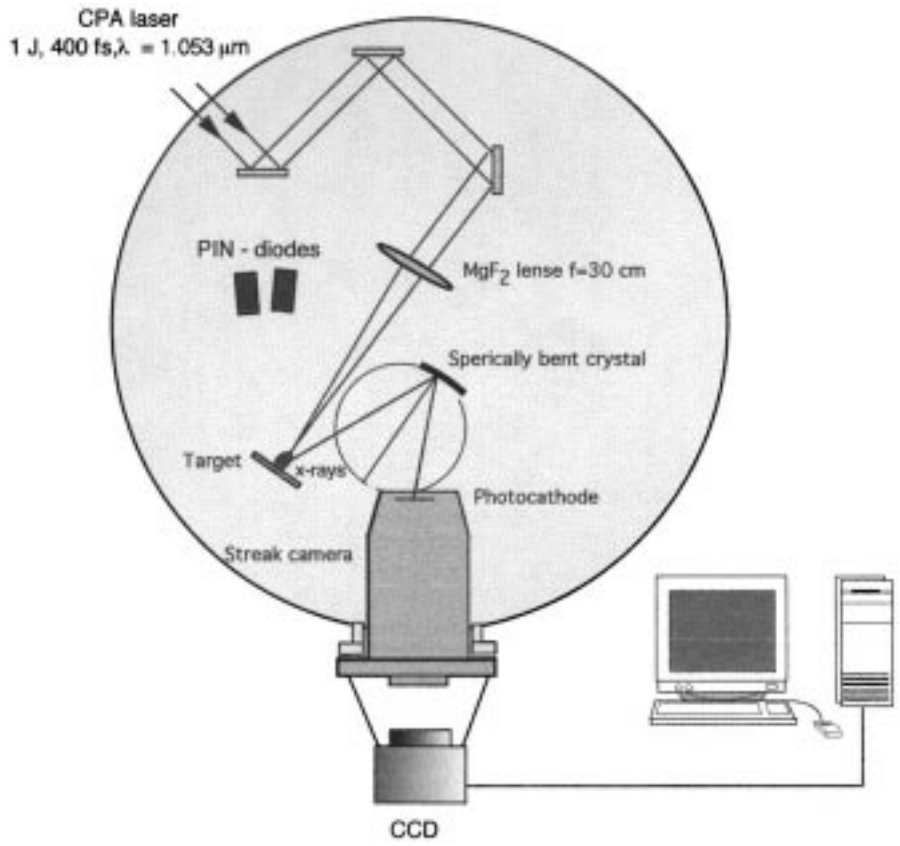


Fig. 10. Experimental setup for time resolved emission spectroscopy using spherically curved X-ray crystal and an X-ray streak camera in a slitless mode.

Introducing the equivalent Einstein coefficients $A_{s1,s2}(\omega')$, Eq. (3.1) can be rewritten as

$$P_{s1,s2} = \hbar\omega' N_{\mathrm{f}} A_{\mathrm{L}}(\omega'), \tag{3.3}$$

where

$$A_{s1,s2}(\omega') = I_{\mathrm{L}}\sigma/(\hbar\omega_{\mathrm{L}}). \tag{3.4}$$

When the energy $\hbar\omega'$ of the emitted photon falls in the X-ray range, the probabilities $A_{s1}(\omega_{fg} + \omega_{\mathrm{L}})$ and $A_{s2}(\omega_{fg} - \omega_{\mathrm{L}})$ are practically identical and therefore both laser satellites should have approximately equal intensities. The line intensity ratio of the laser satellite to the resonance transition $r \to g$ (for optically thin plasma) is

$$\frac{P_{s1,s2}}{P_r} = \frac{\omega' N_f A_{s1,s2}(\omega')}{\omega_{rg} N_r \quad A_{rg}}. \tag{3.5}$$

The population ratio $N_f/N_r$ was modeled by FLY [40]. The density dependence of the ratio of the intensities of the laser satellites to the intensity of the resonance line for several laser intensities and

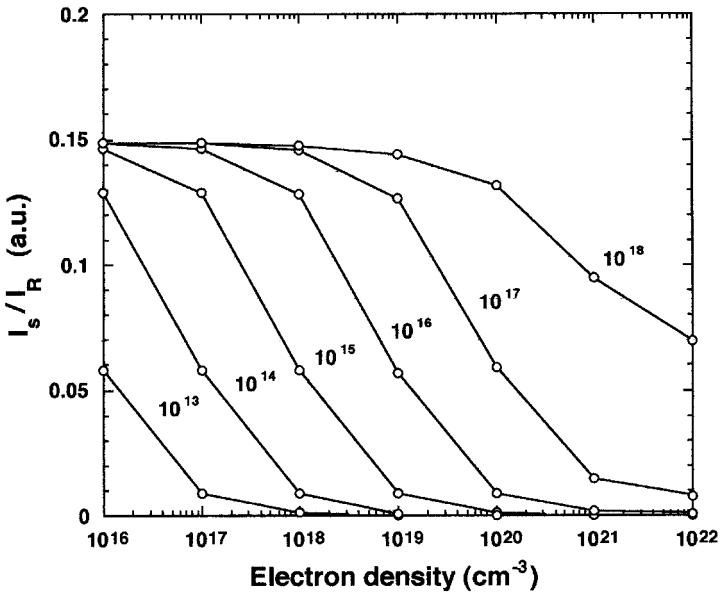


Fig. 11. He-like magnesium laser satellite ($1s2s^1S_0$–$1s^2\ ^1S_0$) to resonance line ratio for different laser intensities.

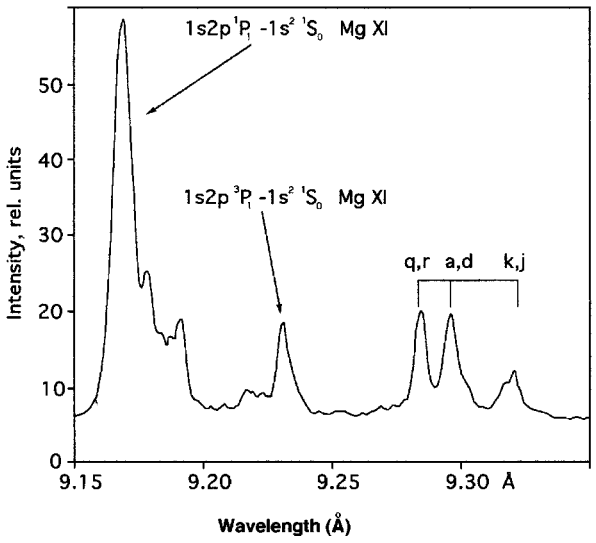


Fig. 12. Time integrated emission spectrum of magnesium plasma, produced by high-intensity subpicosecond laser pulse.

for an electron temperature of 200 eV is shown in Fig. 11. The intensity of the laser satellite can reach 15% of the resonance line, comparable with the intensities of Li-like satellites. The saturation of the laser satellite intensity for low plasma densities and laser intensities above $10^{14}$W/cm$^2$ is due to the large laser-induced decay rate of the $2^1S_0$ level, which dominates the collisional decay. When

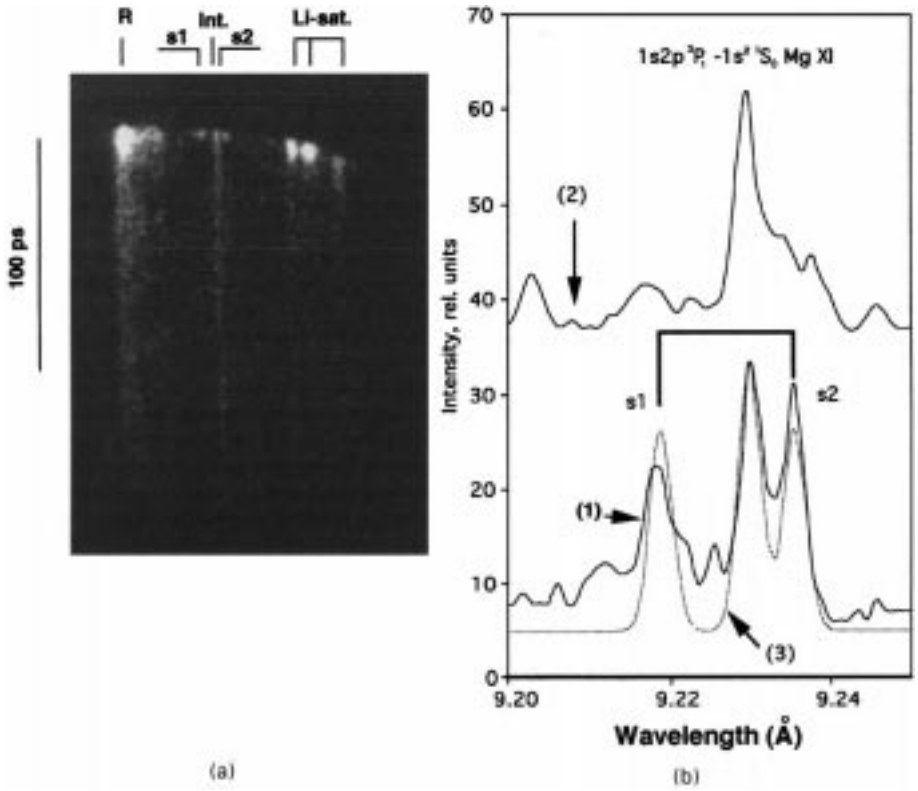


Fig. 13. (a) Temporally and spectrally resolved Mg XI X-ray emission. Curvature of the streaked image is due to the shortest path for the photoelectrons travelling on-axis of a streak camera. (b) Corresponding line-outs during the laser pulse (1) and immediately after the pulse (2). Curve (3) is a result of theoretical modeling.

the electron density increases the collisional decay rate quenches the laser-induced decay. It should be pointed out that the laser satellites are emitted only during the laser pulse $\tau_L$ while the standard spectral lines are emitted during the plasma lifetime $\tau_{plasma}$. The latter one is determined by the hydrodynamic processes of plasma expansion and in the case of low contrast illumination of the solid target with ultrashort laser pulse can be as long as a few tens and even hundred of picosecond [47]. If the spectra are recorded without temporal resolution the time integrated ratio of the laser satellites to the resonance line will be significantly reduced in proportion to $\tau_L/\tau_{plasma}$, so the satellites intensity will not exceed the noise level of spectrograms.

The time-integrated emission spectrum of a magnesium plasma in the spectral range 9.15–9.35 Å received in a static mode of the X-ray streak camera operation is shown in Fig. 12 and illustrates the points just made. The identified lines are He-like resonance line ($1s2p^1P_1$–$1s^2\ ^1S_0$), intercombination line ($1s2p^3P_1$–$1s^2\ ^1S_0$) and Li-like satellites ($1s^2$–$1s3l3l'$). The spectrum is quite similar to that observed for nanosecond laser-produced plasma and does not show any unusual features. The spectrum has significantly changed for the dynamic mode of the X-ray streak camera operation (Fig. 13). We observed in the vicinity of the intercombination line two additional lines with the wavelengths of 9.2199 and 9.2366 Å which are clearly visible only during the laser pulse (Fig. 13a).

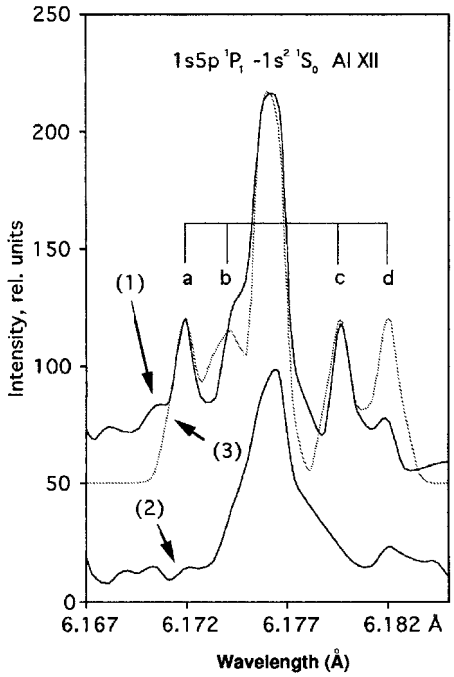


Fig. 14. Emission from the aluminum plasma during the laser pulse (1) and immediately after the pulse (2). Curve (3) is a result of theoretical modeling.

Fig. 13b shows the line-outs of the spectrum during the laser pulse (curve 1) and 10 ps after the laser pulse (curve 2). Fig. 13b shows also the model spectrum constructed for the electron temperature of 200 eV and electron density of $10^{21}$ cm$^{-3}$ [48]. As in the case of the time integrated spectrum (Fig. 11), the laser satellites are similarly absent after the heating pulse ends (curve 2 in Fig. 13b), while during the laser pulse (curve 1) their position and intensity agree well with the theoretical estimates (curve 3).

Similar results are also obtained for the laser satellites of the $1s5p^1P_1$–$1s^2\ ^1S_0$ line of the He-like ion Al XII (Fig. 14). In this case it was possible to observe four laser satellites, which are due to the interaction of the laser photons with $1s5d^1D_2$ state (spectral lines a,c) and the $1s5s^1S_0$ state (spectral lines b,d). The modeled spectrum [48] for the plasma in coronal equilibrium with temperature $T_e \simeq 200$ eV is also presented in (Fig. 14) (curve 3).

Since $E_f(\mathrm{cm}^{-1}) = 10^8(1/\lambda_{s1}(\mathring{\mathrm{A}}) + 1/\lambda_{s2}(\mathring{\mathrm{A}}))$, the detection of laser satellites provides a direct method for measuring the excitation energies of the metastable levels of ions. We found good agreement between the values of excitation energy of the metastable levels $1s2s^1S_0$ of MgXI, $1s5s^1S_0$ and $1s5d^1D_2$ of AlXII (see Table 1) with that predicted theoretically [49].

In summary, the detection of X-ray emission from plasma with picosecond time resolution achieved in the present work made it possible to observe laser satellites excited by a high-intensity subpicosecond laser. The fact, that the spectral lines are emitted only during the laser pulse indicates unequivocally that the lines are produced by the nonlinear interaction of laser photons with the exited states of multiply charged magnesium and aluminum ions.

Table 1
Energies of metastable states of the He-like ions Mg XI and Al XII

| Ion | Level | Laser satellite | | Energy ($cm^{-1}$) | |
|---|---|---|---|---|---|
| | | Transition | $\lambda_{exp}$(Å) | Experiment | Theory |
| Mg XI | $1s2s^1S_0$ | $1s2s^1S_0 - 1s^2\ ^1S_0 + \omega_L$ | 9,2199(11) | $1{,}0836(3)\cdot 10^7$ | $1{,}0839\ \cdot 10^7$ |
| | | $1s2s^1S_0 - 1s^2\ ^1S_0 - \omega_L$ | 9,2366(11) | | |
| Al XII | $1s5s^1S_0$ | $1s5s^1S_0 - 1s^2\ ^1S_0 + \omega_L$ | 6,1732(8) | $1{,}6188(3)\cdot 10^7$ | $1{,}6188\ \cdot 10^7$ |
| | | $1s5s^1S_0 - 1s^2\ ^1S_0 - \omega_L$ | 6,1813(8) | | |
| Al XII | $1s5d^1D_2$ | $1s5d^1D_2 - 1s^2\ ^1S_0 + \omega_L$ | 6,1712(8) | $1{,}6194(3)\cdot 10^7$ | $1{,}6192\ \cdot 10^7$ |
| | | $1s5d^1D_2 - 1s^2\ ^1S_0 - \omega_L$ | 6,1789(8) | | |

The study of laser satellites has several important implications. First, the observation of laser satellites makes it possible to perform direct measurements of the excitation energies of the metastable states of the atoms. Second, the intensities of laser satellites can be used to measure the intensity of the laser field in a plasma. Third, since the laser satellites are emitted only during the interaction with the heating pulse, they can be used to produce a source of ultrashort X-ray pulses. Finally, this effect can be employed in a cross-correlation technique to measure the pulse duration of another ultrashort X-ray source.

## 4. Conclusion

We presented here studies of hot dense matter, produced by high-intensity ultrashort laser pulses. In particular, we investigated the effects of strong randomly varying fields of neighboring charged particles in solid density plasmas and harmonically oscillating electric fields with a relativistic strength on the emission of multicharged ions. Using high spectral and temporal resolution X-ray and XUV spectroscopy we were able: (i) to observe solid density plasma, confined by the laser radiation pressure; (ii) study the dynamics of strongly coupled plasma with the initial coupling parameter $\Gamma = 1.5$; (iii) observe for the first time laser satellites of the forbidden transitions of He-like magnesium and aluminum ions.

## Acknowledgements

This work was done under the auspices of the Division of Chemical Sciences, Office of Basic Energy Sciences, Office of Energy Research, US Department of Energy with facilities supported by the Center for Ultrafast Optical Science under NSF Grant No. STC PHY 8920108. M. Nantel was supported in part by FCAR fund. We would also like to thank J.B. Workman, J.C. Kieffer and G. Mourou for fruitful discussions, as well as J. Itatani, J. Faure, D. Kaplan for assistance with the experiment. The authors are grateful to F. Rosmej for providing us with the results of simulations prior to the publication.

## References

[1] Strickland D, Mourou G. Opt Commun 1985;56:219.
[2] Maine P, Strickland D, Bado P, Pessot M, Mourou G. IEEE J Quantum Electron 1988;24:398.
[3] Murnane M, Kapteyn HC, Falcone RW. Phys Rev Lett 1989;62:155.
[4] Kieffer JC, Chaker M, Maine JP, Pépin H, Côté CY, Beaudoin Y, Chien C-Y, Coe S, Mourou G, Peyrusse O. Phys Fluids B 1993;5:2676.
[5] Workman J, Maksimchuk A, Liu X, Ellenberger U, Coe JS, Chien C-Y, Umstadter D. Phys Rev Lett 1995;75:2324.
[6] Rousse A, Audebert P, Geindre JP, Falliès F, Gauthier JC, Mysyrowicz A, Grillon G, Antonetti A. Phys Rev E 1994;50:2200.
[7] Nantel M, Ma G, Gu S, Côté CY, Itatani J, Umstadter D. Phys Rev Lett 1998;80:4442.
[8] Liu X, Umstadter D. Phys Rev Lett 1992;69:1935.
[9] Wilks SC, Kruer WL, Tabak M, Langdon AB. Phys Rev Lett 1992;69:1383.
[10] Perry MD, Mourou G. Science 1994;264:917.
[11] Pennington DM, Perry MD, Stuart BC, Boyd RD, Britten JA, Broun CG, Herman SM, Miller JL, Nguyen HT, Shore BW, Tierbohl GL, Yanovsky V. SPIE Proc 1997;3407:490.
[12] Riley D, Gizzi LA, Khattak FY, Mackinnon AJ, Viana SM, Willi Os. Phys Rev Lett 1992;69:3739.
[13] Jiang Z, Kieffer JK, Matter JP, Chaker M, Peyrusse O, Gilles D, Korn G, Maksimchuk A, Coe S, Mourou G. Phys Plasmas 1995;2:1702.
[14] Kieffer JK, Jiang Z, Ikhlef A, Cote CY, Pseyrusse O. J Opt Soc Am B 1996;13:132.
[15] Young BKF, Wilson BG, Price DF, Stewart RE. Phys Rev E 1998;58:4929.
[16] Peyrusse O, Busquet M, Kieffer JC, Jiang Z, Côté CY. Phys Rev Lett 1995;75:3862.
[17] Rogers FJ, Iglesias CA. Science 1994;263:50.
[18] Brush S, Armstrong BH. Proceedings of Workshop on Lowering of the Ionization Potential, JILA Report 79, Univ. of Colorado, Boulder, CO, 1965.
[19] Griem HR. Plasma spectroscopy. New York: McGraw-Hill, 1964.
[20] Lindl JD, Campbell EM, McCrory RL. Phys Today 1992;45:32.
[21] Tabak M, Hammer J, Glinsky ME, Kruer WL, Wilks SC, Woodworth J, Campbell EM, Perry MD, Mason RJ. Phys Plasmas 1994;1:1626.
[22] Berkovsky MA, Kurilenkov YuK, Milchberg HM. Phys Fluids B 1992;4:2423.
[23] Unsold A. Z Astrophys 1948;24:355.
[24] Inglis DR, Teller E. Astrophys J 1939;90:439.
[25] More RM. JQSRT 1982;27:345.
[26] Rosmej FB et al. JQSRT 2000;65:477.
[27] Ichimaru S. Rev Mod Phys 1982;54:1017.
[28] Lee CM, Hauer A. Appl Phys Lett 1978;33:692.
[29] Hammel BA, Keane CJ, Cauble MD, Kania DR, Kilkenny JD, Lee RW, Pasha R. Phys Rev Lett 1993;70:1263.
[30] DaSilva L, Ng A, Godwal BK, Chiu G, Cottet F. Phys Rev Lett 1989;62:1623.
[31] Djaoui A, Hall TA, Eason R, Jackson C, Rose SJ. Plasma Phys Controlled Fus 1989;31:111.
[32] Bradley DK, Kilkenny J, Rose S, Hares JD. Phys Rev Lett 1987;59:2995.
[33] Heading DJ, Bennett GR, Wark JS, Lee RW. Phys Rev Lett 1995;74:3616.
[34] Workman J, Nantel M, Maksimchuk A, Umstadter D. Appl Phys Lett 1997;70:312.
[35] Kyrala GA, Fulton RD, Wahlin EK, Jones LA, Shappert GT, Cobble JA, Taylor AJ. Appl Phys Lett 1992;60:2195.
[36] Itatani J, Faure J, Nantel M, Mourou G, Watanabe S. Opt Commun 1998;148:70.
[37] Maksimchuk A, Kim M, Workman J, Korn G, Squier J, Du D, Umstadter D, Mourou G, Bouvier M. Rev Sci Instrum 1996;67:697.
[38] Côté CY, Kieffer JC, Gallant P, Rebuffie JC, Goulmy C, Maksimchuk A, Mourou G, Kaplan D, Bouvier M. SPIE Proc 1997;2869:956.
[39] Stewart JC, Pyatt Jr KD. Astrophys J 1966; 144:1203.

[40] Lee RW, Whitten BL, Stout II RE. JQSRT 1984;32:91; Lee, RW, Larsen. JT. ibid, 1996;56:535.
[41] Baranger M, Moser B. Phys Rev 1961;123:25.
[42] Riley D, Willi O. Phys Rev Lett 1995;75:4039.
[43] Vinogradov AV, Yukov EA. Sov J Quantum Electron 1974;3:163.
[44] Skobelev IYu, Faenov AYa, Magunov AI, Osterheld A, Young B, Dunn J, Stewart R. Phys Scripta 1997;T73:104.
[45] Elton RC, Griem HR, Welch BL, Osterheld AL, Mancini RC, Knauer J, Pien G, Watt RG, Cobble JA, Jaanimagi PA, Bradley DK, Delettrez JA, Epstein R. JQSRT 1997; 58:559.
[46] Osterheld AL, Young BKF, Dunn J, Stewart RE, Skobelev IYu, Faenov AYa, Magunov AI. JQSRT 1987;58:827.
[47] Maksimchuk A, Workman J, Liu X, Ellenberger U, Coe JS, Chien C-Y, Umstadter D, X-ray lasers 1994. American Institute of Physics Conference Proceedings No.332, New York: AIP Press, 1994.
[48] Pikuz SA, Maksimchuk A, Umstadter D, Nantel M, Skobelev IYu, Faenov AYa, Osterheld A. JETP Lett 1997;66:480.
[49] Boĭko VA, Pal'chikov VG, Skobelev IYu, Faenov AYa. Spectroscopic reference data for atoms and ions [in Russian]. Moscow.:Izd. Standartov, 1988.